The Relationship Between Large Scale Thermospheric Density Enhancements and the Spatial Distribution of Poynting Flux

D. D. Billett[1], G. W. Perry[2], L. B. N. Clausen[3], W. E. Archer[1], K. A. McWilliams[1], S. Haaland[4,8,9], J. P. Reistad[4], J. K. Burchill[5], M. R. Patrick[5], B. K. Humberset[6], B. J. Anderson[7]

[1]Institute of Space and Atmospheric Studies, University of Saskatchewan, Saskatoon, SK, Canada
[2]Center for Solar-Terrestrial Research, New Jersey Institute of Technology, Newark, NJ, USA
[3]Department of Physics, University of Oslo, Oslo, Norway
[4]Birkeland Centre for Space Science, Department of Physics and Technology, University of Bergen, Bergen, Norway
[5]Department of Physics and Astronomy, University of Calgary, Calgary, AB, Canada
[6]Faculty of Humanities and Education, Volda University College, Volda, Norway
[7]Applied Physics Laboratory, Johns Hopkins University, Laurel, Maryland, USA
[8]Max-Planck-Institut für Sonnensystemforschung, Göttingen, Germany
[9]The University Centre in Svalbard, Longyearbyen, Svalbard

Key Points:

- Statistical patterns of the total downward Poynting flux into the atmosphere have been derived using SuperDARN and AMPERE data.
- Statistical patterns of neutral mass density perturbations as a percentage of the background density have been derived using CHAMP data.
- Mesoscale downward Poynting flux in the cusp region do not correlate very well with neutral mass density enhancements at a similar scale.

Corresponding author: D. D. Billett, daniel.billett@usask.ca

Abstract

Large thermospheric neutral density enhancements in the cusp region have been examined for many years. The CHAMP satellite for example has enabled many observations of the perturbation, showing that it is mesoscale in size and exists on statistical timescales. Further studies examining the relationship with magnetospheric energy input have shown that fine-scale Poynting fluxes are associated with the density perturbations on a case-by-case basis, whilst others have found that mesoscale downward fluxes also exist in the cusp region statistically.

In this study, we use nearly 8 years of the overlapping SuperDARN and AMPERE datasets to generate global-scale patterns of the high-latitude and height-integrated Poynting flux into the ionosphere, with a time resolution of two minutes. From these, average patterns are generated based on the IMF orientation. We show the cusp is indeed an important feature in the Poynting flux maps, but the magnitude does not correlate well with statistical neutral mass density perturbations observed by the CHAMP satellite on similar spatial scales. Mesoscale height-integrated Poynting fluxes thus cannot fully account for the cusp neutral mass density enhancement, meaning energy deposition in the F-region or on fine-scales, which is not captured by our analysis, could be the primary driver.

Plain Language Summary

1 Introduction

The density of the neutral thermosphere at high latitudes is primarily modulated by changes in solar irradiance, and by magnetospheric interactions with the solar wind causing energy to transfer down magnetic field lines (Prölss, 2011). The former is regular and predictable, which controls the "background" neutral density, whilst the latter can be considered as a cause of perturbations beyond the background.

The cusp enhancement is a well-known neutral density perturbation in the high-latitude thermosphere. The first observations were by Lühr et al. (2004), who found significantly enhanced neutral densities in the dayside cusp region (∼68-75° geomagnetic latitude, 10-12 magnetic local time) during several passes of the Challenging Minisatellite Payload (CHAMP; Reigber et al., 2002) at around 400 km altitude. It was subsequently shown by H. Liu et al. (2005) and Schlegel et al. (2005) that the cusp enhance-

ment existed even under average conditions and during geomagnetically quiet times, with a 20-30% increase above the background neutral density (i.e. that caused by irradiance), that was not able to be predicted by global circulation models of the neutral winds and densities. These studies ultimately confirmed what had been strongly suspected for a few decades, that solar wind energy was directly influencing the high-latitude upper thermospheric structure. A review of this history up to the early CHAMP observations can be found in Moe and Moe (2008). The mechanism by which the cusp density enhancement is generated is however still not well understood.

A survey of density enhancements seen by CHAMP during geomagnetic storms by R. Liu et al. (2010) found that they are typically less than 900 km in latitudinal width, and occur during all interplanetary magnetic field (IMF) orientations (although greater magnitudes of perturbation tend to occur during negative IMF B_z conditions; Rentz & Lühr, 2008). Lühr et al. (2004) originally attributed the cusp enhancement to intense small scale (∼10s of km) field-aligned currents (FACs) and their associated electric fields, which would drive Joule heating and upwelling of the neutral gas. However, the aforementioned R. Liu et al. (2010) survey found that only around half of events coincided with strong FACs. Simulations by Demars and Schunk (2007) showed that cusp ion heating events would indeed generate a thermospheric upwelling, but only when increasing the ion-neutral frictional heating term by a factor of 110 to simulate extreme events.

In contrast, Clemmons et al. (2008) found a density depletion of a few percent about 150 km below the CHAMP orbital altitude within the dayside cusp vicinity, utilising complementary neutral density data from the Streak mission (Clemmons et al., 2009). The depletion was thought to be indicative of the short (or "soft") penetration depth of particle precipitation in the cusp region, and upon modelling, produced the thermospheric upwelling theorised by previous studies at 400 km altitude (e.g. Demars & Schunk, 2007), but not in the upper E-region. Subsequently, Deng et al. (2011) decoupled the effects of Joule heating deposited at both low (<150 km) and high (>300 km) altitudes, showing that much of the temporal variation of the atmospheric upwelling at CHAMP altitudes (∼ 350-450 km) was caused by low altitude heating. However, F-region Joule heating was primarily responsible for the neutral density and vertical wind enhancements in the F region. This was attributed to the higher heating per unit mass in the F region compared to the E region, and showed that E-region Joule heating that would be associated with FAC closure could not be fully responsible for density enhancements seen

in the F-region. Brinkman et al. (2016) later found, in agreement with the conclusions by Clemmons et al. (2009) and Deng et al. (2011), that the low altitude density depletion was probably due to the neutral gas being transported upwards as the thermosphere expands. Brinkman et al. (2016) also saw soft particle precipitation heating playing an important role in driving a cusp neutral density enhancement.

Crowley et al. (2010) was able to reproduce a cusp enhancement observed by CHAMP using the Assimilative mapping of ionospheric electrodynamics (AMIE; Richmond, 1992) as input to the TIME-GCM (Roble & Ridley, 1994) during an extreme geomagnetic storm. A DMSP satellite, that was included in the assimilation, saw large and localised downward Poynting fluxes in the cusp region during the event. Indeed, Knipp et al. (2011) showed statistically that very large magnitudes of Poynting flux into the cusp were common during events where the IMF magnitude was >10 nT. Deng et al. (2013), utilising the Global Ionosphere-Thermosphere Model (GITM; Ridley et al., 2006), also found that a very large magnitude of Poynting flux imposed on the ionosphere generated a cusp density enhancement by as much as 29% in the F region due to soft particle precipitation and Joule heating. These studies however did not explain the existence of the cusp neutral density enhancement during geomagnetically quiet times. It should also be noted that the total magnitude of Poynting flux when it is dissipated in the ionosphere is split between Joule heating and mechanical work, with Joule heating being dominant most of the time (Thayer et al., 1995). Joule heating, as it is dependent on the Pedersen conductivity, is highest in the E-region, but still has significant effects on the F-region thermosphere due to the low neutral density (Billett et al., 2020), and during cases such as that described by Deng et al. (2013) mentioned previously.

In the empirical model of Poynting flux developed by Cosgrove et al. (2014), the cusp was highlighted as a region of strong downward Poynting flux under northward IMF conditions. This was in stark contrast to previous empirical models, such as that by Weimer (2005), which showed no significant amount of energy in the cusp region under any IMF orientation. This difference was attributed to the use of a separate empirical electric field model in the older studies that would not have captured the variability of the field well, which is a known shortcoming that results in underestimating the total energy dissipation into the ionosphere (e.g. Codrescu et al., 1995). Electric field variability in the cusp region can indeed be high, however the IMF orientation may not be a good descriptor of that variability (Förster et al., 2007; Cosgrove & Thayer, 2006). In the statistical study

of Joule heating by Billett et al. (2018), cusp enhancements were seen to have both a universal time and seasonal dependence, which is more indicative of variations in the dayside conductivity than electric field variability.

In this study, we develop statistical high latitude Poynting flux distributions and compare them to statistical distributions of neutral mass density enhancements. We employ ∼10 years of neutral density measurements from the CHAMP satellite (Reigber et al., 2002; Doornbos et al., 2010), along with global scale calculations of Poynting flux using ∼7 years of data from the Active Magnetosphere and Planetary Electrodynamics Response Experiment (AMPERE; Anderson et al., 2014) and the Super Dual Auroral Radar Network (SuperDARN; Greenwald et al., 1995). Our statistical Poynting flux patterns based on IMF orientation are the first to be created using the combined AMPERE and SuperDARN datasets, whilst neutral density perturbations within the well-established CHAMP dataset are found using a novel technique which highlights the cusp in relation to the surrounding areas. It is shown that whilst our patterns of Poynting flux and neutral mass density perturbations are consistent with many previous studies, there does not appear to be a strong correlation between them in terms of both morphology and magnitude on mesoscales. This implies that at least one underlying process, whether because it is happening at a smaller scale or otherwise, is not being captured by our analysis.

2 Data

2.1 Neutral Density Perturbation

The CHAMP satellite was launched in 2000 into a nearly circular orbit which gradually decreased from an altitude of approximately 450 km until it re-entered the Earth's atmosphere in 2010. The accelerometer on board CHAMP enabled the detection of neutral mass density perturbations as small as $1 \times 10^{-14}\,\mathrm{kg\,m^{-3}}$, with a time resolution of 10 s. The full pre-processed dataset of neutral densities over the entire lifetime of CHAMP, including positional information, can be obtained from Förster and Doornbos (2019). Due to the variations in altitude, previous studies utilising CHAMP measurements have typically normalised neutral densities to a common altitude using models for the thermospheric scale height (e.g. H. Liu et al., 2005). We have instead derived neutral mass density perturbations from a running average 'background' density, i.e. a deviation from the

density which is driven by solar EUV flux, similar to the method employed by Clemmons et al. (2008) and Clausen et al. (2014).

For a neutral mass density point measurement made by CHAMP (ρ), a background neutral mass density $\langle\rho\rangle$, which is made up of an average of the previous 5 minutes of measured densities, is subtracted. This background density spans approximately 20° of magnetic latitude along the CHAMP orbital track, or 30 measurements. The calculated value is then normalised as a fraction of the background neutral mass density, giving a perturbation mass density ($\Delta\rho$) that is in terms of fractional percent:

$$\Delta\rho = \frac{\rho - \langle\rho\rangle}{\langle\rho\rangle} \tag{1}$$

$\Delta\rho$ will hold both temporal and spatial perturbations. However, the timescale upon which the thermospheric density changes is almost certainly several hours longer than the 5 minutes captures by the background density average, for all altitudes seen by CHAMP (Wilson et al., 2006; Sutton et al., 2009; Wang et al., 2020). Therefore, $\Delta\rho$ is almost entirely a measure of how the region of interest compares to the region the satellite has just passed through. A 5-minute timescale for $\langle\rho\rangle$ is short enough that large scale features, such as density enhancements due to changing solar irradiance with proximity to the sub-solar point, should be mostly removed from $\Delta\rho$.

As the CHAMP dataset spans many years, encompassing both the peak of solar cycle 23 and a portion of the cycle 24 incline, it is important that the significant effects of solar EUV on the neutral mass density (Walterscheid, 1989) is minimised in our results. Using this method for determining a perturbation neutral mass density, rather than looking at altitude-normalised densities, almost entirely removes the effect of changing solar flux (e.g. the $f_{10.7}$ radio emission) due to only sampling the past 5 minutes of data for each data point. Additionally, the short timescale used also minimises seasonal and altitude density variations. This process does very well at extracting only density changes that are due to spatial inhomogeneities, but is subsequently unable to show temporal changes in a particular region due to events such as substorms unless the density change happens unprecedentedly fast. Substorms are unlikely to have a significant effect on cusp neutral densities however, as they are primarily a nightside phenomenon.

In this study, we have binned $\Delta\rho$ from the entire CHAMP dataset into an equal area (∼200×400 km) grid poleward of 60° latitude in altitude-adjusted corrected geomagnetic coordinates (AACGM; Shepherd, 2014). Each grid cell is 2° tall in AACGM

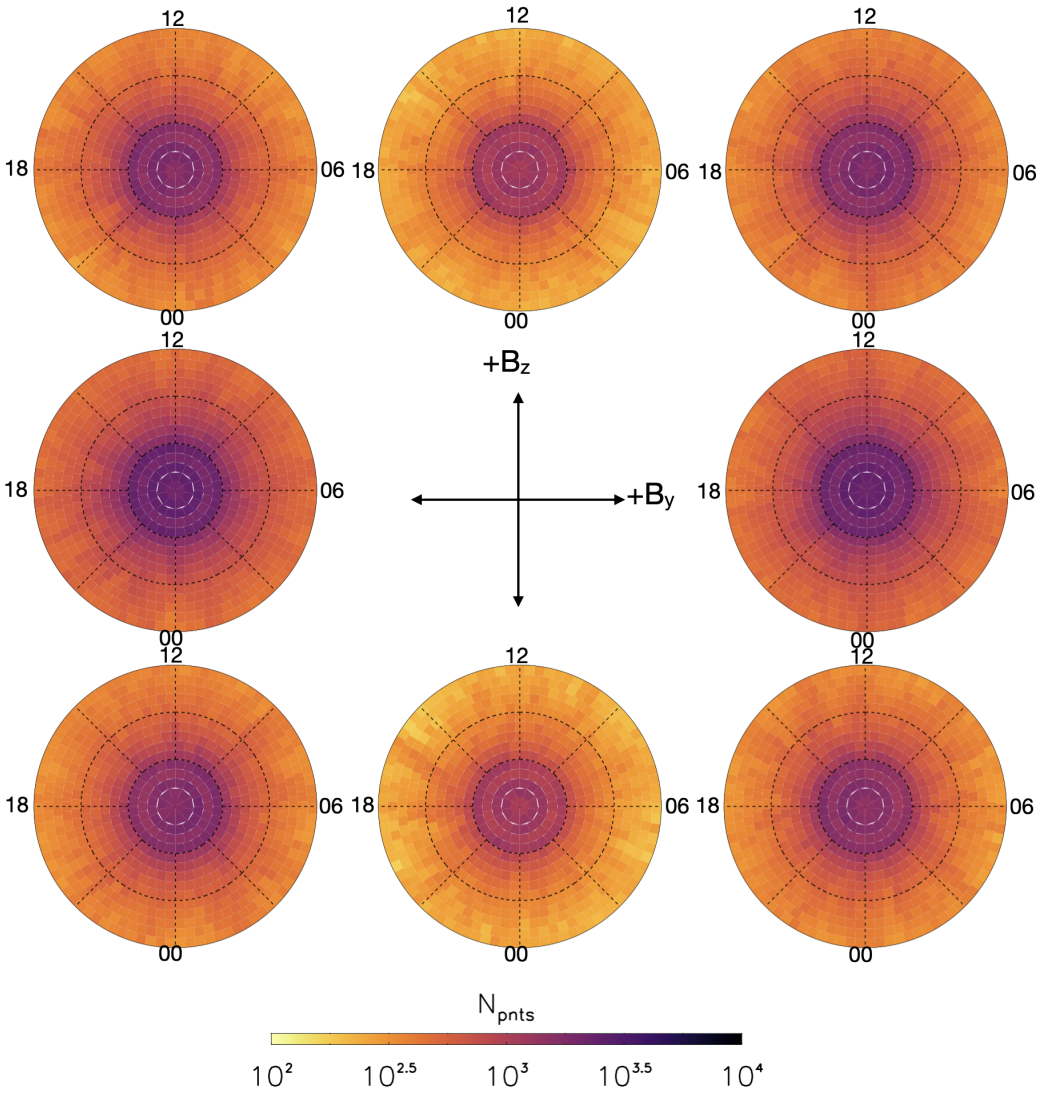

Figure 1. Distribution of CHAMP neutral mass density measurements in AACGM MLat-MLT coordinates, upwards of 60° MLat, sorted by IMF clock angle sector. Concentric circles are seperated by 10° latitude and the MLT is displayed around the outside of each plot.

latitude with increasing longitudinal width a s the grid nears the AACGM north pole. The data has also subsequently been binned into 8 IMF clock angle sectors, defined by the angle the IMF B_y and B_z vector makes in geocentric solar magnetospheric (GSM) coordinates. The IMF information is taken at the point of measurement using the 1-minute resolution OMNI dataset (retrieved from `http://omniweb.gsfc.nasa.gov`) and is time-shifted from the measuring spacecraft to the Earth (King & Papitashvili, 2005). The distribution of CHAMP measurements used in this study for each clock angle bin is shown

in Figure 1, in terms of AACGM latitude and magnetic local time (MLT). Of note is that there is less data in the purely northward and southward B_z sectors, and more data closer to the AACGM pole where CHAMP orbits tend to overlap. The clock angle during the 5 minutes involved in calculating $\langle\rho\rangle$ is not accounted for in the IMF binning, but we have found that imposing a filter to use only periods of steady IMF does not significantly affect the spatial distribution of $\Delta\rho$. Even a low-pass steady IMF filter of just a few minutes however, such as that employed by Haaland et al. (2007) to remove 'unsteady' IMF periods, significantly reduces the amount of data available in our analysis. We have therefore opted to show unfiltered results from here on.

2.2 Poynting Flux

The perturbation Poynting vector $\mathbf{S}_{||}$, i.e. the total amount of energy dissipated in the ionosphere via FACs, is given by Waters et al. (2004):

$$\mathbf{S}_{||} = -\frac{1}{\mu_0}\left(\mathbf{E} \times \delta\mathbf{B}\right) \cdot \hat{\mathbf{r}} \tag{2}$$

where μ_0 is the permeability of free space, $\mathbf{E}$ is the ionospheric electric field, $\delta\mathbf{B}$ is the perturbation magnetic field (deviation from the terrestrial field) and $\hat{\mathbf{r}}$ is the unit vector parallel to the geomagnetic field. $\mathbf{S}_{||}$ is positive downward, indicating the magnetosphere is driving the ionosphere. Negative (or upward) Poynting flux indicates that the ionosphere might be driving the magnetosphere as a current generator through the ionospheric wind dynamo. We obtain electric field information from the SuperDARN and perturbation magnetic field measurements from AMPERE, both on a global scale, combining them using equation 2 and the method described by Waters et al. (2004) onto the same grid used for neutral density perturbations.

Overlapping AMPERE and SuperDARN data currently exists between years, 2010 and 2017, and like the neutral density binning process, we have also not filtered the times for steady IMF conditions. However, it is important to note that by not filtering the AMPERE and SuperDARN datasets in this way, we do not account for the fact that the ionosphere does not immediately and fully respond to a change in IMF driving conditions (Murr & Hughes, 2001). This will generally mean that statistical Poynting fluxes during southward (northward) IMF orientations are slight underestimations (overestimations) because they include values calculated during variable IMF conditions.

2.2.1 Electric field

The Super Dual Auroral Radar Network (SuperDARN; Greenwald et al., 1995; Chisham et al., 2007; Nishitani et al., 2019) consists of 36 (as of 2020) high-frequency radars in both the northern and southern hemispheres. Line-of-sight doppler velocities of the F-region (∼250 km altitude) plasma are measured by each radar within a large field-of-view spanning a few thousand kilometres, which are then all gridded together based on hemisphere. A spherical harmonic fit (Ruohoniemi & Greenwald, 1996) is applied to the gridded velocities to solve for the instantaneous global electrostatic potential, Φ, which is related to the ionospheric electric field by $\mathbf{E} = -\nabla\Phi$. Using the electric potential solution, the full electric field vector can be calculated at any position in a hemisphere, which is what was done for each grid cell used for the CHAMP data binning. When using SuperDARN data in this way however, it is also common to employ an empirical electric potential model (e.g. Thomas & Shepherd, 2018) that is based on the IMF to 'fill in the gaps' for regions where SuperDARN velocity data is scarce. This however can potentially introduce occasions where the global maps of Φ are very dependent on the empirical model if there is not enough input data. In this study, we have utilised the Thomas and Shepherd (2018) model in the maps of electric potential that were used, but only during times where 200 or more gridded SuperDARN data points were available in the map. This means that only maps with a significant amount of measured data constraining the spherical harmonic fit to Φ were included. 200 points is generally good enough to ensure a reasonable spread of data globally, whilst reducing the amount of 'usable' map data by around 55% (Billett et al., 2018). Maps are made using integrations of 2 minutes.

2.2.2 Perturbation magnetic field

The Active Magnetosphere and Planetary Electrodynamics Response Experiment (AMPERE; Anderson et al., 2014) uses magnetometers on board the Iridium satellite constellation to derive global maps of both the northern and southern hemisphere FACs. The in-situ magnetic field at around 780 km altitude is sampled, then perturbations caused by FACs ($\delta\mathbf{B}$) are determined by subtracting the Earth's magnetic field using the IGRF model (Thébault et al., 2015). Further corrections are then made to account for various sensor biases, residuals and noise (Anderson et al., 2000). Finally, values are normalised to an altitude of 250 km (to match the assumed altitude of SuperDARN mea-

surements) to account for the convergence of magnetic field lines with decreasing altitude (using the 3/2 relationship described by Knipp et al., 2014).

$\delta\mathbf{B}$ is gridded with respect to AACGM coordinates spaced 1° in latitude and 1 hour (15°) of magnetic local time, with a time resolution of 2 minutes and integration window of 10 minutes. Subsequently binning the magnetic perturbations onto the same grid used for the CHAMP data involved iterating over each AMPERE grid cell, then binning each data point onto every overlapping CHAMP grid cell. Cells with two or more $\delta\mathbf{B}$ were then averaged over each timestep.

3 Results

Figure 2 shows the average perturbation neutral density ($\Delta\rho$) patterns for 8 IMF clock angle orientations, derived using equation 1 and the entirety of the CHAMP data set above 60° AACGM latitude. Immediately noticeable under all IMF orientations is a positive enhancement of several percent above the background neutral density in the region between 70-80° MLat and 7-14 MLT. The enhancement looks to be slightly smaller under positive B_z conditions, and there is a B_y dependence on its asymmetry around magnetic local noon where it shifts towards the dawnside under positive B_y conditions.

For all patterns of $\Delta\rho$, there is a depletion region between 1-6 MLT, encompassing anywhere from ∼10-25° of latitudinal width depending on the IMF orientation. The latitudinal thickness of the depletion appears to also have a B_y dependence, where positive values show a latitudinally thinner region. This might explain why the depletion for the purely B_y positive pattern is much weaker than the others, such that it is more difficult to pick out from the surrounding areas. For patterns where B_z is negative, there is an additional moderate $\Delta\rho$ depletion of around 80° MLat centred on magnetic local dusk. In all other regions for all patterns, $\Delta\rho$ has a low magnitude on average compared to the more distinct regions just described.

Figure 3 shows the average Poynting flux ($\mathbf{S}_{||}$) patterns derived using equation 2 with SuperDARN and AMPERE data. It is important to note here that the CHAMP data set does not overlap with the AMPERE dataset, therefore the $\mathbf{S}_{||}$ and $\Delta\rho$ averages are calculated from different timespans. Both however are calculated from ∼7 and ∼10 years worth of data, respectively, thus should give accurate statistical representations. The number of two-minute Poynting flux maps which were used in the averaging for each

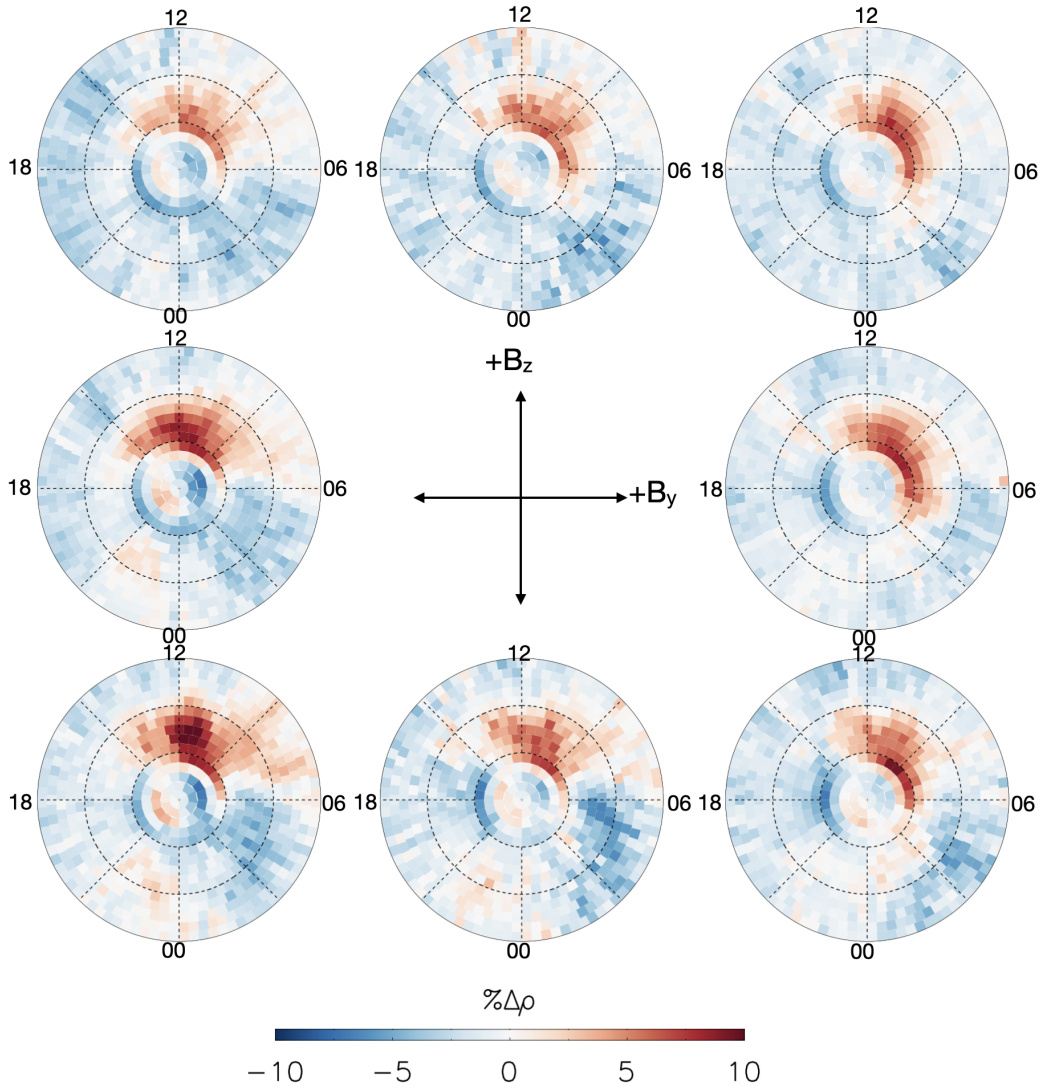

Figure 2. Average perturbation neutral densities ($\Delta\rho$) for the entirety of the CHAMP neutral mass density dataset, in the same format as Figure 1.

statistical pattern are shown in the centre of Figure 3, ranging from a minimum of $\sim 45\times10^3$ maps to a maximum $\sim 85\times10^3$ maps used, depending on IMF orientation. Negative (upward) Poynting fluxes have also not been shown in Figure 3 because their magnitude, on average, is exceedingly small compared to positive values in all regions (i.e. downward into the ionosphere). This is because on average it would be expected, and is clearly apparent in our results, that the magnetosphere drives the ionosphere and not vice versa (Gary et al., 1995).

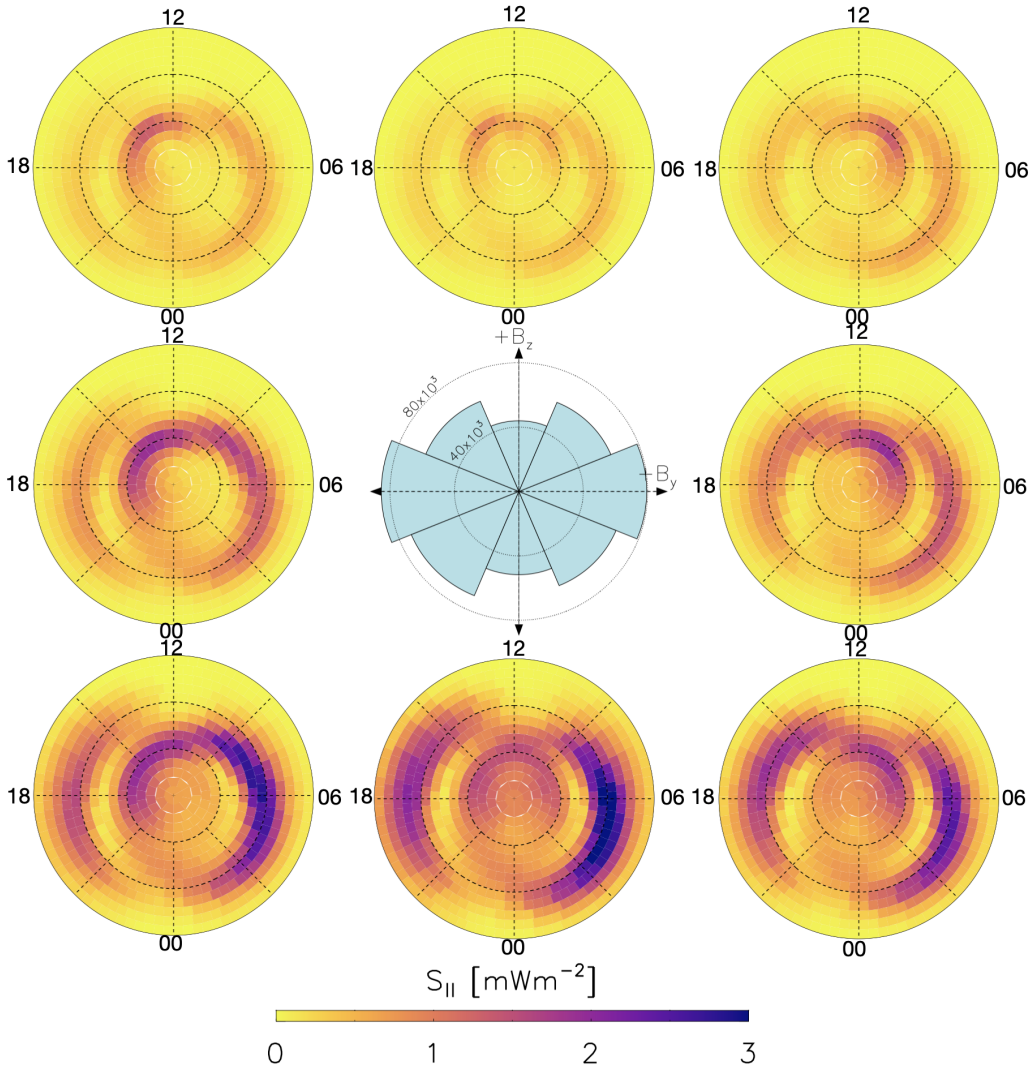

Figure 3. Average Poynting flux ($\mathbf{S}_{||}$) calculated using AMPERE perturbation magnetic fields and SuperDARN electric fields between 2010 and 2017, in the same format as Figure 2. Only positive values are shown (downward flux), because negative (upward) fluxes were minuscule on average compared to the positive values. The centre IMF dial also shows the number of Poynting flux maps that went into each average, marked with indicator circles at 80×10^3 and 160×10^3 maps.

Larger than surrounding area values are seen in the high-latitude ~78-82° MLat dayside region for all patterns (which we henceforth refer to as the cusp region), the local time extent of which is highly controlled by the IMF B_y component. The B_y positive patterns have a strong cusp region enhancement that is shifted towards dawn, whilst the enhancement under B_y negative patterns is shifted towards dusk. For all $\mathbf{S}_{||}$ patterns

in Figure 3, enhancements of downward flux are also seen on both the dawn and dusk sides between 60 and 75° MLat, the dawnside enhancements being consistently stronger for all IMF orientations. Overall magnitudes of $\mathbf{S}_{||}$ are much greater for the negative IMF B_z patterns in general when compared to positive B_z, and the aforementioned dawn and dusk enhancements extend to lower latitudes under negative B_z conditions.

4 Discussion

Our statistical patterns of the perturbation neutral mass density, $\Delta\rho$, shown in Figure 2 clearly show the cusp neutral density enhancement. As it is observable during both geomagnetically quiet and active times however (H. Liu et al., 2005; Kwak et al., 2009), this is not a particularly surprising result. Both Yamazaki et al. (2015a) and Yamazaki et al. (2015b) showed very similar results, but expressed their neutral densities as perturbations from a quiet time state. Our values in contrast include both quiet and active times, showing that the neutral density in the cusp region is always enhanced by several percent above the surrounding regions, for all IMF orientations and magnitudes. It is also worth mentioning that the negative neutral density perturbation in the dawnside region we show is a well known thermospheric feature that is thought to be caused by downward winds, in response to a traditional cyclonic plasma convection cell on the dawnside (Crowley et al., 1996; Guo et al., 2019). It was originally predicted by the Crowley et al. (1996) model that the dawnside depletion would not be detectable at CHAMP altitudes. Previous studies involving CHAMP data however, including ours, do show its existence. Schlegel et al. (2005) hypothesised that the discrepancy might be caused by either imperfect upper boundary conditions, or the non-inclusion of wave motions within the model.

A key similarity our results share with the studies previously mentioned is that under northward IMF B_z conditions, the cusp enhancement is still a prominent feature of the high-latitude thermosphere. Although, $\Delta\rho$ only considers the surrounding areas for a given IMF orientation. Therefore, even though the neutral mass density is very likely lower in magnitude when the IMF B_z is positive (e.g. Yamazaki et al., 2015a), the cusp enhancement still exists as an approximately constant percentage enhancement above the background for all other IMF orientations. Thus, the forcing which is responsible for the neutral mass density enhancements in the cusp is probably also responsible for the density surrounding the cusp. However, it is not clear whether $\Delta\rho$ that exists statisti-

cally under northward IMF is a result of forcing which occurs during northward IMF, or simply the result of "lingering" enhanced densities from previous forcing. Timescales for thermospheric density changes are usually on the order of several hours, but the IMF clock angle often varies on the order of minutes, meaning the thermosphere may not often have enough time to fully respond to an IMF change.

The SuperDARN/AMPERE statistical patterns of downward Poynting flux in Figure 3 are consistent with previous modelling and observational results (e.g. McHarg et al., 2005; Weimer, 2005; Zhang et al., 2005; Deng & Ridley, 2007; Cosgrove et al., 2014), i.e., distinct regions of high downward flux on the dawn and dusk sides where the convection electric field, and thus Joule heating, is high. Many of these studies have also shown patterns binned by IMF orientation that displayed a very large decrease in downward Poynting flux magnitude over the entire hemisphere when B_z is positive compared to negative, in agreement with our results. Figure 3 also shows that downward Poynting flux is higher on the dawnside compared to the duskside below $\sim$75° MLat, which is consistent with enhanced dawnside Joule heating due to neutral winds opposing the direction of plasma convection (Billett et al., 2018). It is not surprising that every pattern in Figure 3 has a perceptible cusp region Poynting flux enhancement above background levels, as Milan et al. (1998) showed that the F-region dayside cusp is a "hard target" for the SuperDARN radars, meaning it is commonly observable regardless of changing ionospheric conditions.

The empirical Poynting flux model by Cosgrove et al. (2014) shows the cusp to be an important feature under northward IMF conditions. Cosgrove et al. (2014) attributed this deviation from previous studies as an indication of electric field variability in the cusp region which could not be captured with empirical models. Electric field measurements from the SuperDARN used in this study were however not averaged; each individual two-minute integrated electric field map was paired with a perturbation magnetic field map from AMPERE to derive an instantaneous global Poynting flux map. Therefore, the variability of the electric field that the SuperDARN map fitting process calculates is preserved. Given, there is a degree of "smoothing out" of the electric potential spatially when the spherical harmonic fit is applied to radar velocity data, but this does not affect the SuperDARNs ability to detect small temporal electric field variability on the order of minutes (Cousins & Shepherd, 2012a, 2012b). Regardless, the IMF B_z positive patterns in Figure 3 do indeed show that downward Poynting flux in the cusp region is higher than

that in the 60-75° MLat dawn and dusk regions (i.e. the auroral zone), whilst the opposite is true when B_z is negative. This is in general agreement with the Cosgrove et al. (2014) model, however the magnitudes shown here are not as large. Downward Poynting fluxes in the cusp region during northward IMF are however highly sensitive to the IMF magnitude (Li et al., 2011; Lu et al., 2018), which could mean the averages shown in Figure 3 are weighted down by Poynting flux patterns with low IMF magnitudes. Additionally, the Cosgrove et al. (2014) model utilises significantly finer time resolution electric field measurements than those used in this study (<0.25 s vs 2 minutes), which could potentially have resolved electric fields associated with the fine-scale FACs that Lühr et al. (2004) saw alongside the cusp density enhancement originally. The bin sizes used for our statistical patterns are also very much within the region of mesoscales (∼100s of square kilometres in area), so they would not resolve the effects of small and fine-scale phenomena.

To better compare our results of Poynting flux enhancements and neutral mass density perturbations in the cusp region, Figure 4 shows all binned values of $\mathbf{S}_{||}$ (black) and $\Delta\rho$ (red) between MLTs of 11-13 and AACGM latitudes of 60-90°, for each IMF orientation. The MLT range was chosen to be 2 hours wide around magnetic local noon to isolate the cusp region, but also so that large Poynting fluxes from the dawn and dusk side enhancement regions (seen for all patterns in Figure 3) were not introduced.

$\Delta\rho$ peaks at AACGM latitudes as low as 75° (bottom right plot) and as high as 81° (top right plot), which is very consistent with the cusp neutral mass density enhancement locations seen by Lühr et al. (2004) and later authors. There is also a high-latitude peak of $\mathbf{S}_{||}$ that is distinct and near the $\Delta\rho$ peaks for most IMF orientations. In general, downward Poynting flux appears to maximise 2-4° above neutral mass density perturbations in latitude, being closest when the IMF B_y is positive.

It is interesting to see in Figure 4 that even though peaks in $\mathbf{S}_{||}$ occur approximately in a similar region to peaks in $\Delta\rho$, their magnitudes do not appear closely correlated. For example, the cusp peak of $\Delta\rho$ is approximately the same when B_z is both positive and negative (with zero B_y), but the Poynting flux is larger by around a factor of two when the IMF is southward compared to northward. This might because a short term (10s of minutes) injection of downward Poynting flux near the cusp would result in the neutral density in the same region to become enhanced for several hours (e.g. Sutton et

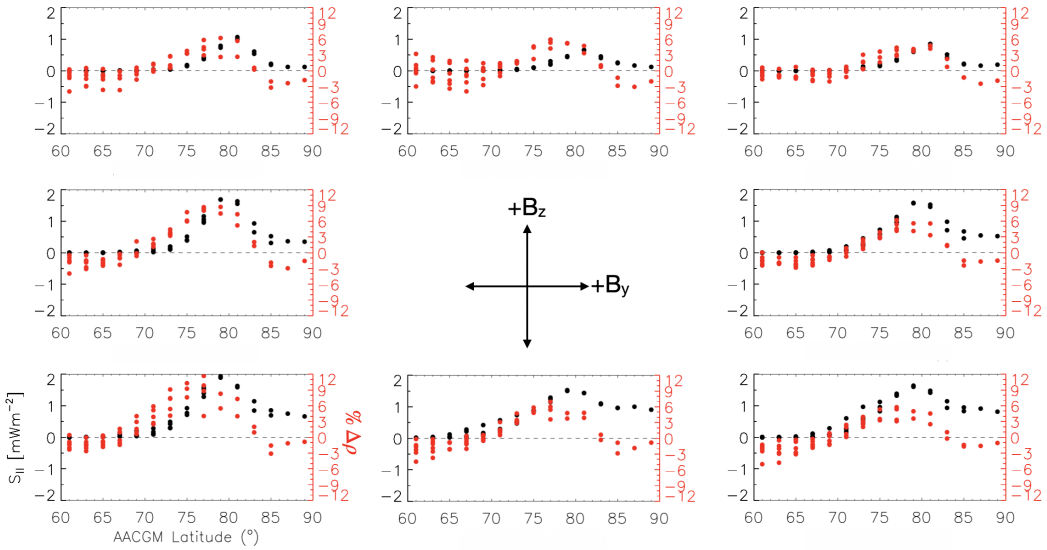

Figure 4. Binned values of $\Delta\rho$ (red) and $\mathbf{S}_{||}$ (black) from Figures 2 and 3 between 11-13 MLT and 60-90° AACGM latitude.

al., 2009; Wang et al., 2020). The discrepancy between how short a time the Poynting flux is enhanced and how long the neutral mass density is enhanced would cause the patterns of $\Delta\rho$ to be biased towards strong geomagnetic events, whilst $\mathbf{S}_{||}$ would be biased towards quiet geomagnetic times which are more frequent than large events such as those seen by Crowley et al. (2010) and Knipp et al. (2011).

We also note that $\Delta\rho$ is larger in the cusp region when the IMF B_y is negative compared to positive, but $\mathbf{S}_{||}$ is of a similar magnitude when B_y is both positive and negative (for the same B_z). Yamazaki et al. (2015a) saw the same neutral density asymmetry in their results, but focused mainly on discussing its effect on the dawnside density depletion region (also seen in Figure 3). It is clear that both $\Delta\rho$ and $\mathbf{S}_{||}$ in the cusp region have a significant local time dependency on B_y (e.g. in Figures 2 and 3), however the local time extent of cusp enhancements, in addition to the magnitudes, do not correlate well. For example, cusp region $\mathbf{S}_{||}$ extends much further onto the duskside during B_y negative conditions, but the corresponding $\Delta\rho$ pattern is fairly symmetric around noon. If enhanced downward Poynting fluxes were indeed a 1:1 correlation with enhanced neutral densities on these spatial scales, then co-rotation of thermospheric neutrals would cause density perturbations much further onto the duskside than is seen in Figure 2 for negative B_y patterns.

As $\Delta\rho$ is in terms of the neutral mass density in surrounding areas, it is reasonable to interpret any cusp perturbation to be due to solar wind energy input variations and not due to "background processes" that affect the density such as solar EUV dissociation/recombination. Our calculations of the Poynting flux based on SuperDARN and AMPERE data however do not totally explain the cusp density enhancement based on magnitude alone, also factoring the bias in $\Delta\rho$ towards strong events. This could be because fine scale FAC structures such as those initially seen by Lühr et al. (2004) are simply not captured by AMPERE or SuperDARN because the spatial bin size is too large and the temporal integration too long. The mesoscale downward Poynting flux averages captured by our patterns (on the order of $\sim$1000 km spatial resolution) indicate that enhancements in the general cusp region are at least common enough to be statistically significant, but are perhaps not the main driver behind neutral mass density enhancements on a similar scale. Alternatively, it could be a result of the vastly different response timescales between the thermosphere and ionosphere that causes $\Delta\rho$ and $\mathbf{S}_{||}$ to appear not well correlated statistically.

The altitudinal dependence of Poynting flux deposition in the thermosphere is an important factor that is not considered in our analysis. We effectively only show the total altitude integrated downward Poynting flux, as both the SuperDARN velocities and AMPERE magnetic field measurements used are from F-region altitudes (>250 km). Most of the energy included in our statistical averages will be deposited at E-region altitudes where the Pedersen conductivity is high, but it has been shown that the smaller amount of energy deposition in the F-region is enough to drive thermospheric upwelling and winds at the same altitude due to soft particle precipitation and low neutral densities (Clemmons et al., 2008; Deng et al., 2011; Brinkman et al., 2016; Billett et al., 2020). We cannot make a conclusion as to the mechanism by which mesoscale downward Poynting flux contributes to mesoscale neutral density perturbations, but as it is mostly E-region dissipated flux, it perhaps contributes most to the temporal variation of the cusp neutral density, as per the modelling results by Deng et al. (2011) showing that to be the case.

5 Summary

Using the CHAMP dataset, we have produced statistical patterns of the perturbation neutral mass density based on IMF orientation. Our technique is novel, as the perturbations are expressed as a percentage of the instantaneous background neutral mass

density for each CHAMP orbit. We have also for the first time generated statistical patterns of the total downward Poynting flux into the atmosphere utilising the combined SuperDARN and AMPERE datasets, from the technique described originally by Waters et al. (2004). The well-known dayside cusp neutral density enhancement was examined on mesoscales and compared to the calculated Poynting flux. It was found that:

- Neutral mass density perturbations of several percent above background levels exist in the dayside cusp regions for all orientations of the IMF. The perturbation above the background density is larger when the IMF B_y is negative.
- There is an enhancement of the total downward Poynting flux in the cusp region for all orientations of the IMF, but it is considerably higher globally when the IMF B_z is negative. Under positive B_z conditions, downward Poynting flux in the cusp is higher than that in the lower latitude auroral zone. The local time maximum of cusp region Poynting flux is highly dependent on the IMF B_y.
- Total downward Poynting fluxes at mesoscales on average do not appear to fully correlate with average neutral mass density perturbations on the same scale, e.g. the morphology and magnitude differences between patterns for different IMF orientations. This could be because most of the height integrated Poynting flux is deposited in the E region, thus fine-scale high-magnitude F-region energy deposition is not captured. Additionally, thermospheric response timescales on the order of hours could be masking the effect of enhanced Poynting fluxes, which is highly dependent on IMF and thus varies on the order of minutes.

It is clear from our results and comparisons with previous studies and empirical models that using the AMPERE and SuperDARN datasets in this way to derive global patterns of total Poynting flux is powerful. However, they are limited in that the coarse spatial resolution of AMPERE and SuperDARN fitted data products is not appropriate for the study of small-scale phenomena, which may in this study have been the reason that Poynting flux averages did not correlate well with the neutral mass density perturbation averages. There is scope to further utilise the SuperDARN-AMPERE method to examine Poynting flux on a global scale, such as to estimate the morphology and magnitude of Joule heating during case studies, but it would also be possible to increase the spatial resolution substantially in a localised region by using data from individual SuperDARN radars and Iridium satellites.

Acknowledgments

This research was supported by the National Sciences and Engineering Research Council of Canada (NSERC). DDB was supported by NSERC CREATE Grant #479771-20, whilst KM was supported by NSERC Discovery Grant #RGPIN 05472-2017. The authors acknowledge the use of data from SuperDARN, an international project made possible by the national funding agencies of Australia, Canada, China, France, Italy, Japan, South Africa, Norway, the United Kingdom and the United States of America. SuperDARN data can be downloaded from Globus, instructions of which are provided here: `https://superdarn.ca/data-products`. SuperDARN data in this study was processed using the Radar Software Toolkit (RST), version 4.3: `https://github.com/SuperDARN/rst`. We also thank the AMPERE team and the AMPERE Science Center for providing the Iridium derived data products, which can be plotted and downloaded at: `http://ampere.jhuapl.edu/`. CHAMP pre-processed neutral density measurements and positional information was obtained from the GFZ Potsdam data repository at `http://doi.org/10.5880/GFZ.1.1.2019.001`.

References

Anderson, B. J., Korth, H., Waters, C. L., Green, D. L., Merkin, V. G., Barnes, R. J., & Dyrud, L. P. (2014). Development of large-scale Birkeland currents determined from the Active Magnetosphere and Planetary Electrodynamics Response Experiment. *Geophysical Research Letters*, *41*(9), 3017–3025.

Anderson, B. J., Takahashi, K., & Toth, B. A. (2000). Sensing global Birkeland currents with Iridium® engineering magnetometer data. *Geophysical Research Letters*, *27*(24), 4045–4048.

Billett, D. D., Grocott, A., Wild, J. A., Walach, M.-T., & Kosch, M. J. (2018). Diurnal variations in global Joule heating morphology and magnitude due to neutral winds. *Journal of Geophysical Research: Space Physics*, *123*(3), 2398–2411.

Billett, D. D., McWilliams, K. A., & Conde, M. G. (2020). Colocated Observations of the E and F Region Thermosphere During a Substorm. *Journal of Geophysical Research: Space Physics*, *125*(11), e2020JA028165. doi: https://doi.org/10.1029/2020JA028165

Brinkman, D. G., Walterscheid, R. L., Clemmons, J. H., & Hecht, J. H. (2016).

High-resolution modeling of the cusp density anomaly: Response to particle and Joule heating under typical conditions. *Journal of Geophysical Research: Space Physics*, *121*(3), 2645–2661.

Chisham, G., Lester, M., Milan, S. E., Freeman, M. P., Bristow, W. A., Grocott, A., ... Walker, A. D. M. (2007). A decade of the Super Dual Auroral Radar Network (SuperDARN): scientific achievements, new techniques and future directions. *Surveys in Geophysics*, *28*(1), 33-109. doi: 10.1007/s10712-007-9017-8

Clausen, L. B. N., Milan, S. E., & Grocott, A. (2014). Thermospheric density perturbations in response to substorms. *Journal of Geophysical Research: Space Physics*, *119*(6), 4441-4455. doi: https://doi.org/10.1002/2014JA019837

Clemmons, J. H., Friesen, L. M., Katz, N., Ben-Ami, M., Dotan, Y., & Bishop, R. L. (2009). The ionization gauge investigation for the Streak mission. *Space science reviews*, *145*(3-4), 263–283.

Clemmons, J. H., Hecht, J. H., Salem, D. R., & Strickland, D. J. (2008). Thermospheric density in the earth's magnetic cusp as observed by the streak mission. *Geophysical Research Letters*, *35*(24). doi: 10.1029/2008GL035972

Codrescu, M. V., Fuller-Rowell, T. J., & Foster, J. C. (1995). On the importance of E-field variability for Joule heating in the high-latitude thermosphere. *Geophysical Research Letters*, *22*(17), 2393–2396.

Cosgrove, R. B., Bahcivan, H., Chen, S., Strangeway, R. J., Ortega, J., Alhassan, M., ... others (2014). Empirical model of Poynting flux derived from FAST data and a cusp signature. *Journal of Geophysical Research: Space Physics*, *119*(1), 411–430.

Cosgrove, R. B., & Thayer, J. P. (2006). Parametric dependence of electric field variability in the Sondrestrom database: A linear relation with Kp. *Journal of Geophysical Research: Space Physics*, *111*(A10).

Cousins, E. D. P., & Shepherd, S. G. (2012a). Statistical characteristics of small-scale spatial and temporal electric field variability in the high-latitude ionosphere. *Journal of Geophysical Research: Space Physics*, *117*(A3).

Cousins, E. D. P., & Shepherd, S. G. (2012b). Statistical maps of small-scale electric field variability in the high-latitude ionosphere. *Journal of Geophysical Research: Space Physics*, *117*(A12).

Crowley, G., Knipp, D. J., Drake, K. A., Lei, J., Sutton, E., & Lühr, H. (2010).

Thermospheric density enhancements in the dayside cusp region during strong BY conditions. *Geophysical Research Letters*, *37*(7).

Crowley, G., Schoendorf, J., Roble, R. G., & Marcos, F. A. (1996). Cellular structures in the high-latitude thermosphere. *Journal of Geophysical Research: Space Physics*, *101*(A1), 211-223. doi: 10.1029/95JA02584

Demars, H. G., & Schunk, R. W. (2007). Thermospheric response to ion heating in the dayside cusp. *Journal of atmospheric and solar-terrestrial physics*, *69*(6), 649–660.

Deng, Y., Fuller-Rowell, T. J., Akmaev, R. A., & Ridley, A. J. (2011). Impact of the altitudinal Joule heating distribution on the thermosphere. *Journal of Geophysical Research: Space Physics*, *116*(A5).

Deng, Y., Fuller-Rowell, T. J., Ridley, A. J., Knipp, D., & Lopez, R. E. (2013). Theoretical study: Influence of different energy sources on the cusp neutral density enhancement. *Journal of Geophysical Research: Space Physics*, *118*(5), 2340–2349.

Deng, Y., & Ridley, A. J. (2007). Possible reasons for underestimating Joule heating in global models: E field variability, spatial resolution, and vertical velocity. *Journal of Geophysical Research: Space Physics*, *112*(A9).

Doornbos, E., Van Den Ijssel, J., Luhr, H., Forster, M., & Koppenwallner, G. (2010). Neutral density and crosswind determination from arbitrarily oriented multiaxis accelerometers on satellites. *Journal of Spacecraft and Rockets*, *47*(4), 580–589.

Förster, M., Paschmann, G., Haaland, S. E., Quinn, J. M., Torbert, R. B., Vaith, H., & Kletzing, C. A. (2007). High-latitude plasma convection from Cluster EDI: variances and solar wind correlations. *Annales Geophysicae*, *25*(7), 1691-1707. Retrieved from `https://hal.archives-ouvertes.fr/hal-00318357`

Förster, M., & Doornbos, E. (2019). *Upper thermosphere neutral wind cross-track component deduced from CHAMP accelerometer data.* `http://doi.org/10.5880/GFZ.1.1.2019.001`. doi: 10.5880/GFZ.1.1.2019.001

Gary, J. B., Heelis, R. A., & Thayer, J. P. (1995). Summary of field-aligned Poynting flux observations from DE 2. *Geophysical research letters*, *22*(14), 1861–1864.

Greenwald, R. A., Baker, K. B., Dudeney, J. R., Pinnock, M., Jones, T. B., Thomas,

E. C., ... Yamagishi, H. (1995). Darn/Superdarn: A Global View of the Dynamics of High-Lattitude Convection. *Space Science Reviews*, *71*(1-4), 761-796. doi: 10.1007/BF00751350

Guo, D., Lei, J., Ridley, A., & Ren, D. (2019). Low-density cell of the thermosphere at high latitudes revisited. *Journal of Geophysical Research: Space Physics*, *124*(1), 521-533. doi: 10.1029/2018JA025770

Haaland, S. E., Paschmann, G., Förster, M., Quinn, J. M., Torbert, R. B., McIlwain, C. E., ... Kletzing, C. A. (2007). High-latitude plasma convection from cluster edi measurements: method and imf-dependence. *Annales Geophysicae*, *25*(1), 239–253. doi: 10.5194/angeo-25-239-2007

King, J. H., & Papitashvili, N. E. (2005). Solar wind spatial scales in and comparisons of hourly Wind and ACE plasma and magnetic field data. *Journal of Geophysical Research: Space Physics*, *110*(A2).

Knipp, D. J., Eriksson, S., Kilcommons, L., Crowley, G., Lei, J., Hairston, M., & Drake, K. (2011). Extreme Poynting flux in the dayside thermosphere: Examples and statistics. *Geophysical Research Letters*, *38*(16).

Knipp, D. J., Matsuo, T., Kilcommons, L., Richmond, A., Anderson, B., Korth, H., ... Parrish, N. (2014). Comparison of magnetic perturbation data from LEO satellite constellations: Statistics of DMSP and AMPERE. *Space Weather*, *12*(1), 2–23.

Kwak, Y.-S., Richmond, A. D., Deng, Y., Forbes, J. M., & Kim, K.-H. (2009). Dependence of the high-latitude thermospheric densities on the interplanetary magnetic field. *Journal of Geophysical Research: Space Physics*, *114*(A5).

Li, W., Knipp, D. J., Lei, J., & Raeder, J. (2011). The relation between dayside local poynting flux enhancement and cusp reconnection. *Journal of Geophysical Research: Space Physics*, *116*(A8).

Liu, H., Lühr, H., Henize, V., & Köhler, W. (2005). Global distribution of the thermospheric total mass density derived from CHAMP. *Journal of Geophysical Research: Space Physics*, *110*(A4).

Liu, R., Lühr, H., & Ma, S.-Y. (2010). Storm-time related mass density anomalies in the polar cap as observed by CHAMP. In *Annales geophysicae* (Vol. 28, pp. 165–180).

Lu, Y., Deng, Y., Sheng, C., Kilcommons, L., & Knipp, D. J. (2018). Poynting flux

in the dayside polar cap boundary regions from DMSP F15 satellite measurements. *Journal of Geophysical Research: Space Physics*, *123*(8), 6948–6956.

Lühr, H., Rother, M., Köhler, W., Ritter, P., & Grunwaldt, L. (2004). Thermospheric up-welling in the cusp region: Evidence from CHAMP observations. *Geophysical Research Letters*, *31*(6).

McHarg, M., Chun, F., Knipp, D., Lu, G., Emery, B., & Ridley, A. (2005). High-latitude Joule heating response to IMF inputs. *Journal of Geophysical Research: Space Physics*, *110*(A8).

Milan, S. E., Yeoman, T. K., & Lester, M. (1998). The dayside auroral zone as a hard target for coherent HF radars. *Geophysical research letters*, *25*(19), 3717–3720.

Moe, K., & Moe, M. M. (2008). The high-latitude thermospheric mass density anomaly: A historical review and a semi-empirical model. *Journal of Atmospheric and Solar-Terrestrial Physics*, *70*(5), 794–802.

Murr, D. L., & Hughes, W. J. (2001). Reconfiguration timescales of ionospheric convection. *Geophysical Research Letters*, *28*(11), 2145–2148.

Nishitani, N., Ruohoniemi, J. M., Lester, M., Benjamin, J., Baker, H., Koustov, A. V., ... Kikuchi, T. (2019). Review of the accomplishments of mid-latitude Super Dual Auroral Radar Network (SuperDARN) HF radars. *Progress in Earth and Planetary Science*, *6*(1). doi: 10.1186/s40645-019-0270-5

Prölss, G. W. (2011). Density perturbations in the upper atmosphere caused by the dissipation of solar wind energy. *Surveys in Geophysics*, *32*(2), 101–195.

Reigber, C., Lühr, H., & Schwintzer, P. (2002). Champ mission status. *Advances in space research*, *30*(2), 129–134.

Rentz, S., & Lühr, H. (2008). Climatology of the cusp-related thermospheric mass density anomaly, as derived from CHAMP observations. In *Annales geophysicae* (Vol. 26, pp. 2807–2823).

Richmond, A. D. (1992). Assimilative mapping of ionospheric electrodynamics. *Advances in Space Research*, *12*(6), 59–68.

Ridley, A. J., Deng, Y., & Toth, G. (2006). The global ionosphere–thermosphere model. *Journal of Atmospheric and Solar-Terrestrial Physics*, *68*(8), 839–864.

Roble, R. G., & Ridley, E. C. (1994). A thermosphere-ionosphere-mesosphere-electrodynamics general circulation model (TIME-GCM): Equinox solar cycle

minimum simulations (30–500 km). *Geophysical Research Letters*, *21*(6), 417–420.

Ruohoniemi, J. M., & Greenwald, R. A. (1996). Statistical patterns of high-latitude convection obtained from Goose Bay HF radar observations. *Journal of Geophysical Research: Space Physics*, *101*(A10), 21743–21763.

Schlegel, K., Lühr, H., St.-Maurice, J.-P., Crowley, G., & Hackert, C. (2005, July). Thermospheric density structures over the polar regions observed with CHAMP. *Annales Geophysicae*, *23*(5), 1659-1672.

Shepherd, S. G. (2014). Altitude-adjusted corrected geomagnetic coordinates: Definition and functional approximations. *Journal of Geophysical Research: Space Physics*, *119*(9), 7501–7521.

Sutton, E. K., Forbes, J. M., & Knipp, D. J. (2009). Rapid response of the thermosphere to variations in Joule heating. *Journal of Geophysical Research: Space Physics*, *114*(A4).

Thayer, J. P., Vickrey, J. F., Heelis, R. A., & Gary, J. B. (1995). Interpretation and modeling of the high-latitude electromagnetic energy flux. *Journal of Geophysical Research: Space Physics*, *100*(A10), 19715–19728.

Thébault, E., Finlay, C. C., Beggan, C. D., Alken, P., Aubert, J., Barrois, O., ... others (2015). International geomagnetic reference field: the 12th generation. *Earth, Planets and Space*, *67*(1), 79.

Thomas, E. G., & Shepherd, S. G. (2018). Statistical patterns of ionospheric convection derived from mid-latitude, high-latitude, and polar SuperDARN HF radar observations. *Journal of Geophysical Research: Space Physics*, *123*(4), 3196–3216.

Walterscheid, R. L. (1989). Solar cycle effects on the upper atmosphere-Implications for satellite drag. *Journal of Spacecraft and Rockets*, *26*(6), 439–444.

Wang, X., Miao, J., Aa, E., Ren, T., Wang, Y., Liu, J., & Liu, S. (2020). Statistical Analysis of Joule Heating and Thermosphere Response during Geomagnetic Storms of Different Magnitudes. *Journal of Geophysical Research: Space Physics*, *125*(8), e2020JA027966.

Waters, C. L., Anderson, B. J., Greenwald, R. A., Barnes, R. J., & Ruohoniemi, J. M. (2004). High-latitude poynting flux from combined Iridium and SuperDARN data.

671 Weimer, D. R. (2005). Improved ionospheric electrodynamic models and applica-
672 tion to calculating Joule heating rates. *Journal of Geophysical Research: Space*
673 *Physics*, *110*(A5).
674 Wilson, G. R., Weimer, D. R., Wise, J. O., & Marcos, F. A. (2006). Response of the
675 thermosphere to Joule heating and particle precipitation. *Journal of Geophysi-*
676 *cal Research: Space Physics*, *111*(A10).
677 Yamazaki, Y., Kosch, M. J., & Sutton, E. K. (2015a). A model of high-latitude ther-
678 mospheric density. *Journal of Geophysical Research: Space Physics*, *120*(9),
679 7903–7917.
680 Yamazaki, Y., Kosch, M. J., & Sutton, E. K. (2015b). North-south asymmetry of
681 the high-latitude thermospheric density: IMF BY effect. *Geophysical Research*
682 *Letters*, *42*(2), 225–232.
683 Zhang, X. X., Wang, C., Chen, T., Wang, Y. L., Tan, A., Wu, T. S., ... Wang,
684 W. (2005). Global patterns of Joule heating in the high-latitude ionosphere.
685 *Journal of Geophysical Research: Space Physics*, *110*(A12).